Check for updates

Anion-tethered interface engineering enabling dendrite-free lithium metal anodes†

Lanlan Zuo, Xu Fan, Hang Yu, Di Lu, Peitao Xiao, Xianxian Shi, Chunman Zheng [iD] * and Yufang Chen [iD] *

A functionalized fiber separator with an anion-sieving effect facilitates rapid Li^+ transfer and guides ordered Li deposition. The *in situ* integration of metal organic frameworks (MOFs) with polyacrylonitrile (PAN) fibers effectively prevents MOF agglomeration, and reduces the high reactivity of $-C\equiv N$ groups with Li anodes. Real-time visualization technology confirms uniform Li deposition behavior. The $Li\|Li$ symmetric cell demonstrates exceptional plating-stripping reversibility at 10 mA cm^{-2}. The $Li\|LiNi_{0.8}Co_{0.1}Mn_{0.1}O_2$ cell exhibits 17% higher capacity retention after 250 cycles than commercial polyolefin separator. This *in situ* chemical modification enables dendrite-free Li metal batteries through separator engineering.

Lithium metal batteries (LMBs) represent the next generation of energy storage devices, providing ultra-high energy density (460–600 W h kg^{-1}) and exceptional fast-charging capability (15–30C).[1,2] The overall performance of LMBs is critically dependent on the cycling stability of lithium (Li) metal anodes, which fundamentally determines the operational lifespan of LMBs. Tailoring a uniform and dense Li deposition layer is essential for Li anodes, but this is also difficult due to the uneven lithium-ion (Li^+) concentration distribution and the disordered Li nucleation sites. Recent advancements in Li anode stability optimization primarily focus on the following directions, including electrolyte engineering,[3] three-dimensional current collector design[4] and artificial solid electrolyte interphase (SEI) layer construction.[5] Metal–organic frameworks (MOFs) are promising materials for next-generation rechargeable batteries due to their high porosity, nanopore confinement effects, and thermal stability.[6,7] For instance, zeolite-like MOFs such as ZIF-67/8, which is constructed from imidazole ligands, exhibit a highly ordered structure and excellent thermal stability similar to

zeolites. These properties are beneficial for applications in gas adsorption,[8] photocatalysis[9] and energy storage.[10]

As a vital component in LMBs, the separators serve as an insulated physical barrier between the cathode and anode, and construct the Li^+ transfer channel.[11] Their performance affects the interface stability and Li^+ transfer kinetics. However, the non-polarity and low porosity of commercial polyolefin separators lead to uneven distribution of Li^+ and sluggish transfer rate. Additionally, the inferior thermal conductivity brings about local high current density and accelerates the growth of Li dendrites.[12] Therefore, polymers rich in polar groups are often considered as one of the most desirable substrate materials for advanced separators. Introducing polar groups coordinated with Li^+ could effectively enhance the transport kinetics of Li^+ and achieve uniform Li deposition. Polymer fibers can also be combined with structurally diverse MOFs, which not only enhance the structural advantages of MOFs, but also avoid side reactions caused by direct contact between strong electron-withdrawing groups and highly active Li. Nevertheless, the mainstream blending method is difficult to control the dispersibility and binding force between the MOFs and the polymer, and the obtained separators are still restricted by insufficient mechanical properties and porosity.[13] Therefore, optimizing the integration strategies of MOFs and polymers, along with elucidating the underlying mechanisms governing Li deposition behaviour, is of critical importance for the development of next-generation LMBs.

Herein, we propose a functionalized fiber separator (N@Co) featuring a rich polar group ($-C\equiv N$) network architecture and an anion-screening effect. By *in situ* growing ZIF-67 on the PAN fibers, the agglomeration of MOFs in conventional blending methods is fundamentally eliminated, and the side reaction between PAN and Li metal is significantly reduced (Fig. S1, ESI†). The open metal sites in ZIF-67 effectively confine the free migration of PF_6^- anions and enhance the Li^+ transfer kinetics. Meanwhile, the dipole–dipole interaction between $-C\equiv N$ groups and $C=O$ in carbonate solvent can form a more stable SEI film. This dual-regulation strategy achieves a superior Li^+ transference number ($t_{Li^+} = 0.8$) and electrochemical stability

Department of Materials Science and Engineering, College of Aerospace Science and Engineering, National University of Defense Technology, Changsha, Hunan 410000, China. E-mail: chenyufang@nudt.edu.cn, zhengchunman@nudt.edu.cn
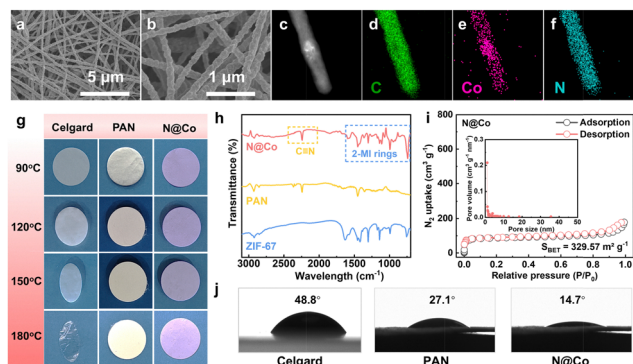
Fig. 1 (a) and (b) SEM and (c) TEM images and corresponding (d)–(f) EDS mapping of the N@Co separator. (g) Photographs of different separators after storage at different temperatures for 0.5 h. (h) FTIR spectra of PAN, N@Co separators and ZIF-67 powder. (i) N_2 adsorption–desorption curve of the N@Co separator (inset: pore size distribution). (j) Contact angle of the ester-based electrolyte on different separators.

window of 4.98 V. The Li∥Li symmetric cell exhibits low overpotential (~ 0.14 V) at 10 mA cm^{-2}. An *in situ* optical microscope recorded the uniform Li deposition behaviours in real time. Accordingly, the Li∥NCM811 cell with the N@Co separator demonstrates a 17% higher capacity retention after 250 cycles than the Celgard separator. This proposal provides a way forward for Li dendrite-free LMBs from the perspective of separator engineering.

Scanning electron microscopy (SEM) images show that cobalt-based MOFs (ZIF-67) are uniformly loaded on a single PAN fiber (denoted as N@Co separator, Fig. 1a and b), and the thickness of the Celgard, PAN and N@Co separators is 20, 30 and 30 μm, respectively (Fig. S2, ESI†). The Celgard separator shows a typical slit-like pore structure (Fig. S3a, ESI†), and the fibers in the PAN separator are smoother compared with the N@Co separator (Fig. S3b, ESI†). The transmission electron microscopy (TEM) image and corresponding energy-dispersive spectrometry (EDS) mapping also revealed the even distribution of elements C, N and Co, with C and N derived from the PAN fiber and Co from the ZIF-67 crystals (Fig. 1c–f). In the Fourier transform infrared spectroscopy (FTIR) of the N@Co separator, the peaks observed at 1200–1500 cm^{-1} and 1300–1600 cm^{-1} correspond to the bending and stretching vibration of the 2-methylimidazole rings (2-MI), respectively.[14] Additionally, the characteristic peak at 2245 cm^{-1} is attributed to the –C≡N group of PAN fibers (Fig. 1h).[15] The X-ray diffraction (XRD) peaks of the N@Co separator at 12.76°, 10.44° and 7.36° belong to the crystal planes (112), (002) and (011) of ZIF-67, respectively (Fig. S4, ESI†).[14] Moreover, the N@Co separator exhibits a 329.57 m^2 g^{-1} increase in BET surface area compared to the PAN separator (14.01 m^2 g^{-1}) (Fig. 1i and Fig. S5b, ESI†), which is attributed to the contribution of ZIF-67 with high specific surface area (498.79 m^2 g^{-1}, Fig. S5a, ESI†). The abundant pore structure is mainly mesopores (see insert). High specific surface area is conducive to improving the electrolyte wettability of the separators. The porosity and electrolyte uptake of the PAN and N@Co separators are increased by (35.7%, 243.8%) and

(47.1%, 404%) compared with the Celgard separator, respectively (Fig. S6, ESI†). Furthermore, the static contact angle of the N@Co separator shows significant advantages, which benefits from the rich polar –C≡N groups and the high porosity of ZIF-67 (Fig. 1j). The stress–strain curve shows that the N@Co separator has superior tensile strength than the PAN separator, which is conducive to withstanding the internal stress caused by electrode volume changes during battery cycling (Fig. S7, ESI†). The excellent thermal stability of the separator ensures the safe operation of the battery under high-temperature conditions. Fig. 1g shows that the PAN and N@Co separators maintain dimensional integrity at 180 °C, whereas the Celgard separator shrinks laterally and becomes transparent. Thermogravimetric curves show the superior thermal stability of the N@Co separator (Fig. S8, ESI†). The residual mass of N@Co separator is about 49.3% at 800 °C, which is significantly higher than that of the Celgard (0%) and PAN (30.4%) separators. This shows that the inclusion of ZIF-67 enhances the thermal stability of the N@Co separator.

Nuclear magnetic resonance (NMR) tests investigate the interaction between ZIF-67 and PF$_6^-$ anions in the electrolyte. For the PF$_6^-$ anion, the ^{19}F and ^{31}P NMR peaks exhibit a significant downfield shift when mixing the electrolyte with the N@Co separator (Fig. 2a and Fig. S9, ESI†). This result indicates a change in the electron cloud density surrounding the F and P atoms, which is attributed to the electrostatic attraction between ZIF-67 and PF$_6^-$ anions.[16] The N@Co separator demonstrates a superior Li$^+$ transference number ($t_{Li^+} = 0.8$) compared to Celgard ($t_{Li^+} = 0.48$) and PAN separators ($t_{Li^+} = 0.65$) (Fig. 2b and c, Fig. S10, ESI†). Additionally, the Li$^+$ conductivity
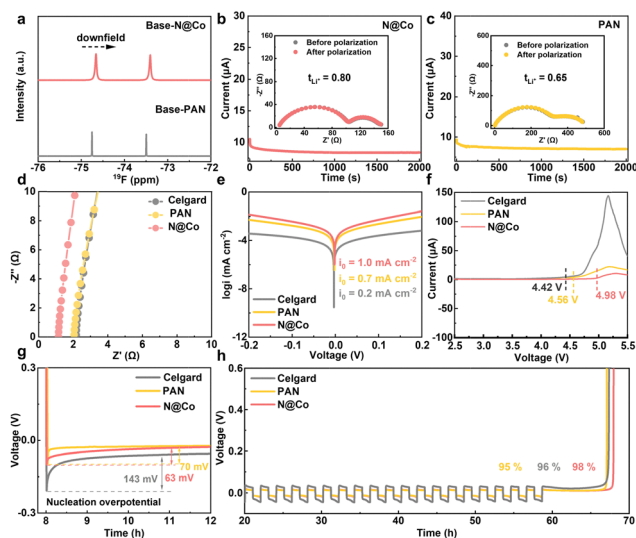

Fig. 2 (a) ^{19}F NMR of the ester-based electrolyte with the N@Co separator (Base-N@Co) and PAN separator (Base-PAN). Potentiostatic polarization test of Li∥Li cells with (b) N@Co and (c) PAN separators (inset: the EIS spectra before and after polarization); (d) Nyquist plots of SS∥SS cells with different separators. (e) Tafel plots of the Li∥Li cells with different separators. (f) Linear sweep voltammetry curves of different separators. (g) The voltage profiles and (h) average coulombic efficiency in Li∥Cu cells with different separators.

of the N@Co separator (1.37 mS cm^{-1}) surpasses that of Celgard (0.48 mS cm^{-1}) and PAN separators (0.77 mS cm^{-1}) (Fig. 2d). These prominent values indicate significantly enhanced Li$^+$ transfer kinetics within the N@Co separator. Furthermore, the exchange current density (i_0) is derived *via* Tafel extrapolation, and quantifies charge transfer kinetics at the electrode–electrolyte interface. The N@Co separator exhibits a higher i_0 value (1.0 mA cm^{-2}) compared to Celgard (0.2 mA cm^{-2}) and PAN (0.7 mA cm^{-2}) separators, reducing the polarization voltage and enhancing the reaction kinetics (Fig. 2e). Linear sweep voltammetry (LSV) investigates the electrochemical stability of the separators soaked in the electrolyte. Compared with the Celgard (4.42 V) and PAN (4.56 V) separators, the electrochemical stability window of the N@Co (4.98 V) separator shows significant improvement (Fig. 2f), indicating that ZIF-67 maintains favorable stability and ameliorates the electrochemical stability of PAN fibers. Moreover, the Li‖Cu half-cells are assembled to evaluate the Li nucleation overpotential and coulombic efficiency (CE).[17] As shown in Fig. 2g, the Li nucleation overpotential is significantly lower in cells with N@Co (63 mV) and PAN separators (70 mV) than Celgard separator (143 mV). The reduced overpotential indicates that the N@Co separator exhibits a lower Li nucleation barrier.[18] Besides, the N@Co-based Li‖Cu half-cell employing ester electrolyte demonstrates a 2% higher average CE compared to the cell with the Celgard separator, indicating improved electrochemical reversibility (Fig. 2h). Notably, the PAN separator shows the lowest average CE (95%), which results from parasitic side reactions between the strong electronegativity –C≡N groups and high activity Li.[19]

To evaluate the compatibility between separators and the Li metal anode, the polarization voltage of Li‖Li symmetrical cells is tested at different current densities (1–10 mA cm^{-2}) with a constant plating capacity (1 mA h cm^{-2}). As the current density increases, the polarization voltage of three Li‖Li symmetrical cells gradually rises (Fig. 3a). This phenomenon results from the limited migration rate of Li$^+$ at high current density, which causes a local concentration gradient on the electrode surface. When the current density reaches 10 mA cm^{-2}, the polarization voltage of the Li‖Li symmetrical cell with Celgard separators suddenly rises, indicating that the cell is short-circuited. Conversely, the Li‖Li symmetrical cell with the N@Co separator exhibits only 142 mV polarization voltage at 10 mA cm^{-2}, while the PAN-based cell undergoes short-circuiting at a lower current density of 6 mA cm^{-2}. The short circuit of the PAN-based cell is attributed to the sluggish Li$^+$ transfer kinetics and parasitic reaction, which lead to local Li$^+$ concentration gradients and uneven Li deposition. Moreover, the N@Co-based Li‖Li symmetrical cell demonstrates stable Li plating and stripping behaviour for over 800 h, maintaining a low polarization voltage of 50 mV without significant fluctuations (Fig. 3b). However, PAN and Celgard-based Li‖Li symmetrical cells exhibit untimely short-circuiting failures during cycling. The difference in the surface and cross-section morphology of the Li anode after cycling demonstrates that the N@Co separator promotes uniform Li deposition. The Li deposition layer with the N@Co separator is smoother and denser than that of the
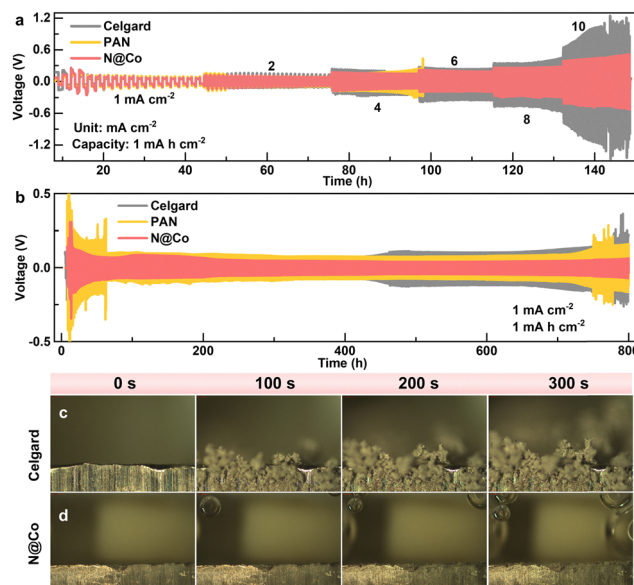

Fig. 3 (a) Rate and (b) long-term cycle performance of Li‖Li symmetric cells with different separators at various current densities with the constant plating capacity of 1 mA h cm^{-2}. Operando optical microscopy investigation of the Li plating behaviour on the Li‖Li symmetric cells with (c) Celgard and (d) N@Co separators at a current density of 5 mA cm^{-2}.

PAN separator, and even delamination occurs with the Celgard separator (Fig. S11, ESI†). Operando optical microscopy (OM) is conducted to monitor the Li deposition behaviour of Li‖Li symmetrical cells with different separators. As shown in Fig. 3c and Fig. S12, ESI,† Li dendrites are observed in the Celgard and PAN separators at 100 s and 200 s, respectively. In contrast, the N@Co separator promotes uniform Li deposition, where the Li deposition layer gradually thickens over time and the Li anode surface remains flat without obvious protrusions and dendrites (Fig. 3d).

As a proof of concept, LMBs with the LiNi$_{0.8}$Co$_{0.1}$Mn$_{0.1}$O$_2$ (NCM811) cathode are assembled to evaluate the applicability of the N@Co separator. Fig. 4a presents the rate capability of LMBs with different separators (1C = 200 mA g^{-1}). The N@Co-based cell demonstrates superior discharge capacity (171 mA h g^{-1}) at 2C, significantly outperforming cells with Celgard (159.8 mA h g^{-1}) and PAN (122.1 mA h g^{-1}) separators. Additionally, the charge–discharge curves reveal that the Li‖NCM811 cell with a N@Co separator shows smaller polarization than Celgard and PAN-based cells, which indicates that the reversibility is more prominent (Fig. 4b, c and Fig. S13, ESI†). The cycling stability testing (Fig. 4d) manifests that the Li‖NCM811 cell with the N@Co separator demonstrates a 17% higher capacity retention after 250 cycles compared to the Celgard separator. Meanwhile, the cell with the PAN separator shows significant capacity fluctuations after 125 cycles, attributed to electrode–electrolyte interfacial degradation and sluggish Li$^+$ transfer. Furthermore, electrochemical impedance spectroscopy (EIS) of the LMBs was carried out to evaluate the interfacial Li$^+$ transfer resistance.[20] The N@Co-based LMB exhibits smaller cell impedance before cycling, which benefits from its good compatibility with the liquid electrolyte.
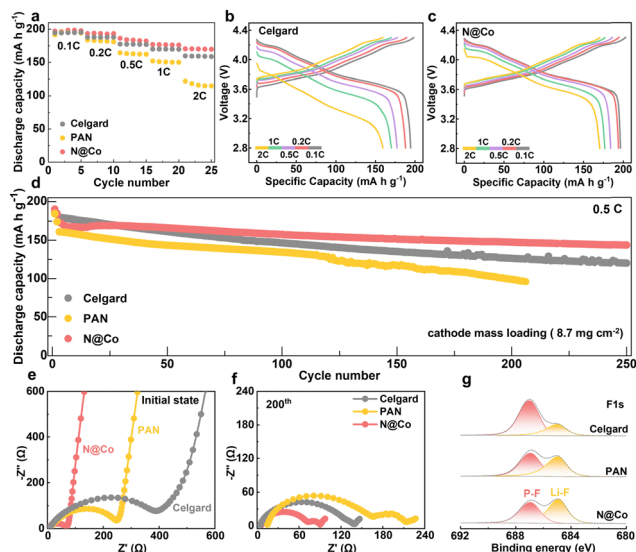
Fig. 4 (a) Rate, (b) and (c) discharge–charge curves and (d) long-term cycling performance of the Li‖NCM811 cells with different separators. The EIS spectra of Li‖NCM811 cells with different separators (e) before and (f) after 200 cycles. (g) The XPS spectra of F1s for the Li anode with different separators after 20 cycles.

After 200 cycles, the high-frequency region resistance (R_{SEI}) of the PAN-based LMB shows a substantial increase (Fig. 4e and f). This suggests sluggish Li$^+$ transfer through the SEI, which is attributed to the accumulation of parasitic reaction by-products. Moreover, X-ray photoelectron spectroscopy (XPS) is performed to ascertain the SEI composition after LMB cycling with different separators. In the F1s spectra, a high percentage of Li–F (685 eV) and a low percentage of P–F (687 eV) peaks are detected on the surface of the Li anode with N@Co separator (Fig. 4g), which are attributed to LiF and decomposition products of LiPF$_6$, respectively.[21] Nevertheless, the P–F peak is dominant in the SEI formed by the PAN and Celgard separators. The XPS results manifest that the N@Co separator can alleviate the decomposition of the electrolyte, and promote the formation of an SEI rich in LiF with high Li$^+$ conductivity. This result illustrates the internal mechanism of the N@Co separator to ensure the long-term stable operation of the LMBs.

In conclusion, the *in situ* integration of MOFs and PAN fibers effectively prevents MOF agglomeration and overcomes the limitations of traditional blending methods. The abundant open metal sites in the MOFs anchor PF$_6^-$ anions, facilitating rapid high-throughput Li$^+$ transfer, which achieves a superior Li$^+$ transference number (t_{Li^+} = 0.8) and Li$^+$ conductivity (σ = 1.37 mS cm^{-1}). Meanwhile, ZIF-67 serves as a protective layer for PAN fibers, mitigating the high reactivity of –C≡N groups with Li anodes, broadening the electrochemical stability window (4.98 V) and reducing interfacial impedance. Consequently, the Li‖Li symmetric cell exhibits remarkable plating and stripping reversibility at 10 mA cm^{-2}. Moreover, the Li‖NCM811 cell demonstrates significantly improved cycling stability. This functionalized fiber separator with anion-sieving effect provides a promising strategy for developing dendrite-free Li metal anodes.

Conflicts of interest

The authors declare no conflict of interest.

Data availability

The data supporting this article have been included as part of the ESI.†

Notes and references

1 S. Zhang, R. Li, T. Deng, Q. Ma, X. Hong, H. Zhang, R. Zhang, S. Ding, Y. Wu, H. Zhu, M. Li, H. Zhang, D. Lu, B. Ma, L. Lv, Y. Li, L. Chen, Y. Shen, R. Guo and X. Fan, *Nat. Energy*, 2024, **9**, 1285–1296.
2 W. Zeng, F. Xia, J. Wang, J. Yang, H. Peng, W. Shu, Q. Li, H. Wang, G. Wang, S. Mu and J. Wu, *Nat. Commun.*, 2024, **15**, 7371.
3 P. Xiao, X. Yun, Y. Chen, X. Guo, P. Gao, G. Zhou and C. Zheng, *Chem. Soc. Rev.*, 2023, **52**, 5255–5316.
4 S. Wang, J. Zhang, L. Zhang, X. Hu, X. Qin, X. Yan, Z. Wang, X. Lu, Y. Xin, F. Kang, H. Tian and B. Li, *Nano Energy*, 2024, **131**, 110255.
5 Z. Wang, Y. Wang, C. Wu, W. K. Pang, J. Mao and Z. Guo, *Chem. Sci.*, 2021, **12**, 8945–8966.
6 H. Zhang, J. Nai, L. Yu and X. W. Lou, *Joule*, 2017, **1**, 77–107.
7 B. Guan, X. Yu, H. Wu and X. W. Lou, *Adv. Mater.*, 2017, **29**, 1703614.
8 L. Shu, Y. Peng, C. Zhu, K. Li and W. Yang, *Nat. Commun.*, 2024, **15**, 10437.
9 J. Wang, J. Zhang, Y. Li, X. Xia, H. Yang, J. Kim and W. Zhang, *Nat. Commun.*, 2025, **16**, 981.
10 Y. An, Z. Pei, D. Luan and X. W. Lou, *Sci. Adv.*, 2025, **11**, eadv2007.
11 Z. Fan, X. Chen, J. Shi, H. Nie, X. Zhang, X. Zhou, X. Xie and Z. Xue, *Nano-Micro Lett.*, 2025, **17**, 128.
12 L. Zuo, Q. Ma, S. Li, B. Lin, M. Fan, Q. Meng, X. Wu, Y. Guo and X. Zeng, *Adv. Energy Mater.*, 2021, **11**, 2003285.
13 L. Y. Yang, J. H. Cao, B. R. Cai, T. Liang and D. Y. Wu, *Electrochim. Acta*, 2021, **382**, 138346.
14 H. Ye, Y. Cao, X. Jin, X. Li, L. Qi, S. Li, R. Yang, Y. Wu, L. Cai, C. Liu and C. Xia, *Adv. Funct. Mater.*, 2025, 2424747.
15 M. Hu, Q. Ma, Y. Yuan, Y. Pan, M. Chen, Y. Zhang and D. Long, *Chem. Eng. J.*, 2020, **388**, 124258.
16 M. Mao, L. Gong, X. Wang, Q. Wang, G. Zhang, H. Wang, W. Xie, L. Suo and C. Wang, *Proc. Natl. Acad. Sci. U. S. A.*, 2024, **121**, e2316212121.
17 B. D. Adams, J. Zheng, X. Ren, W. Xu and J. Zhang, *Adv. Energy Mater.*, 2018, **8**, 1702097.
18 K. Wang, T. Zhao, R. Lv, W. Tang, T. Yu, G. Chen, L. Li, F. Wu and R. Chen, *Adv. Energy Mater.*, 2024, **14**, 2401281.
19 H. Liu, Y. Liao, C. Leung, Y. Zhang, Y. Yang, F. Liu, Y. Wei, C. Fan, S. Zhang, D. Wang, Y. Jan, Q. Liu, C. Chung, Y. Ren, Y. Huang and J. Yang, *Adv. Energy Mater.*, 2024, 2402795.
20 J. Li, L. Shen, Z. Cheng, J. Zhang, L. Li, Y. Zhang, Y. Gao, C. Guo, X. Chen, C. Zhao, R. Zhang and Q. Zhang, *J. Energy Chem.*, 2025, **101**, 16–22.
21 W. Yu, K. Y. Lin, D. T. Boyle, M. T. Tang, Y. Cui, Y. Chen, Z. Yu, R. Xu, Y. Lin, G. Feng, Z. Huang, L. Michalek, W. Li, S. J. Harris, J. C. Jiang, F. Abild Pedersen, J. Qin, Y. Cui and Z. Bao, *Nat. Chem.*, 2025, **17**, 246–255.